Journal of Structural Geology 32 (2010) 1417–1429

Contents lists available at ScienceDirect

Journal of Structural Geology

journal homepage: www.elsevier.com/locate/jsg

The evolution and significance of microfracturing within feldspars in low-grade granitic mylonites: A case study from the Eastern Ghats Mobile Belt, India

Suspa Sinha [a], G. Ian Alsop [b,*], T.K. Biswal [c]

[a] Task Geoscience Ltd., The Enterprise Centre, Aberdeen Science & Energy Park, Exploration Drive, Bridge of Don, Aberdeen, AB23 8GX, UK
[b] Department of Geology and Petroleum Geology, School of Geosciences, University of Aberdeen, Aberdeen AB24 3UE, UK
[c] Department of Earth Sciences, IIT-Bombay, Powai, Mumbai 400076, India

ARTICLE INFO

Article history:
Received 15 January 2010
Received in revised form
12 July 2010
Accepted 24 July 2010
Available online 10 August 2010

Keywords:
Microfractures
Feldspar clasts
Shear zone
Rigid body rotation

ABSTRACT

Patterns of microfracturing are investigated in plagioclase and K-feldspar porphyroclasts formed within granitic mylonites along the boundary of the Eastern Ghats Mobile Belt, India. The mineral assemblage comprising quartz, feldspar, biotite and hornblende suggests lower greenschist facies conditions during mylonitisation, with the contrasting ductile behaviour of quartz and brittle fracturing of feldspars restricting the temperature range during deformation to 300–350 °C. Microfracturing of feldspars takes place by concentration of pure shear within the feldspar-rich layers. This may reflect strain partitioning into dominantly pure and simple shear due to the competency contrasts between the two major constituent minerals (quartz and feldspar). The microfractures occur in conjugates (here designated T_1 and T_2) with T_1 inclined in the same direction as the S-fabric and showing an antithetic sense to the NW verging shear, while T_2 is inclined in an opposite sense to the S-fabric and displays synthetic shear. The direction of maximum compression occurs at high angles to the C-fabric, and the T_1 and T_2 fractures are the result of pure shear localized into brittle layers within the mylonite. With progressive shear, the fractures along with their host feldspar grains are rotated. Theoretical graphs are plotted between bulk shear (γ) and the angle of initiation (α) of T_1 and T_2 with respect to C-planes, for fractures hosted in a circular or elliptical objects. The kinematics of these fractures are also analyzed with regard to variations in shear strain and sense of shear along them. The sense of shear may vary or remain stable within fractures, depending on their initial angle of inclination with respect to the C-fabric. As T_1 is inclined at low angles to the XY plane and in the same direction as the S-fabric, it undergoes maximum shear strain compared to T_2 and may even exceed the bulk shear. This facilitates breakdown of feldspar porphyroclasts during progressive deformation. The T_1 set maintains an antithetic sense of shear even at low angles with the C-fabric, while T_2 displays a synthetic sense in spite of being at high angles to C. The T_1 and T_2 fractures therefore differ significantly from the classic Riedel, *P* and Y shears where low angle fractures display synthetic shear and high angle ones (R') show antithetic displacement with respect to the bulk shear sense.

1. Introduction

It is well established that layered anisotropic rocks may provide strong rheological contrasts which produce coeval brittle and ductile structures during shearing (e.g. Druguet et al., 2009 and references therein). Within granitic rocks, localized high strain zones comprising quartz-rich and feldspar-rich layers may develop even at an early stage of deformation. Park et al. (2006) suggest a dramatic weakening of the bulk rock strength due to the development of such layers, as well as by the breakdown of feldspars into mica. Constituent minerals within shear zones also behave differently during deformation depending on their rheological properties. While some minerals may deform in a ductile manner, others deform as rigid bodies, thus developing a variable microfabric. Quartz and feldspar (plagioclase and K-feldspar) that constitute essential minerals in granite differ significantly in their rheological properties. At low temperature (about 300 °C) and at low strain quartz undergoes ductile deformation, whilst feldspar, even at very high strains, can persist as a brittle mineral. As a consequence, they produce markedly different types of fabric (Goodwin and Tikoff, 2002). Quartz is flattened into lensoidal shapes followed by complete recrystallization producing a grain shape fabric (GSF) (Hirth and Tullis, 1992). Conversely, feldspar exhibits microfracturing and mechanical

* Corresponding author.
E-mail address: Ian.Alsop@abdn.ac.uk (G.I. Alsop).

0191-8141/$ – see front matter © 2010 Elsevier Ltd. All rights reserved.
doi:10.1016/j.jsg.2010.07.006

disintegration with only limited dynamic recrystallization. The quartz GSF is considered so unique that it is utilized as a shear sense indicator (Lister and Snoke, 1984).

Various types and scales of fractures associated with displacement zones have been described in the literature including *R* and *R′* Riedel shears, and *P* and Y shears etc. (see Passchier and Trouw, 2005 for a review). In this paper we report a system of shear fractures (designated T_1 and T_2) that vary in both orientation as well as in sense of shear from those noted above. These are also different from the T-fractures of Petit (1987) that are extensional but lack shear displacement (see Passchier and Trouw, 2005, p. 157). The T_1 and T_2 shear fractures that we describe play an important role in breaking down feldspar porphyroclasts within mylonites. As feldspars rotate with increasing strain, the fractures also rotate passively within them. Slip along these fractures results in strain concentration leading to mechanical disintegration and dynamic recrystallization. They further control the shape of the porphyroclasts and overall fabric of the mylonite.

Although an extensive literature exists on quartz shape and crystallographic fabrics in a simple shear environment, there is much less published material on fabrics produced by the microfracturing of feldspar grains. It is generally believed that microfractures oriented at low angles to the C-foliation, will display shear which is synthetic to the bulk sense of shear (Simpson and Schmid, 1983; Ghosh, 1993). However the present study, both theoretically and from thin section observations, shows that alternative fracture orientations and kinematics are possible during bulk simple shear. This work also emphasizes how these kinematically controlled microfractures help determine the overall fabric asymmetry of mylonites.

2. Regional geological setting

The investigated mylonites formed in the Terrane Boundary Shear Zone (TBSZ) that marks the tectonic contact between the Proterozoic Eastern Ghats Mobile Belt (EGMB) and Archean Peninsular Craton (Biswal and Sinha, 2003, 2004) (Fig. 1). The EGMB comprises supracrustals such as khondalites, charnockitic gneisses, calc granulites, quartzites and banded iron formations, together with some mantle derived intrusive suites. It is characterized by polyphase folding with early generations of folds displaying coaxial folding along an NE–SW axis leading to the overall northwesterly trend of the mobile belt (Biswal et al., 1998). In contrast, the Peninsular Craton consists of tonalite trondhjemite gneisses that have been extensively intruded by late tectonic granite. This late granite lacks any deformational fabric and was

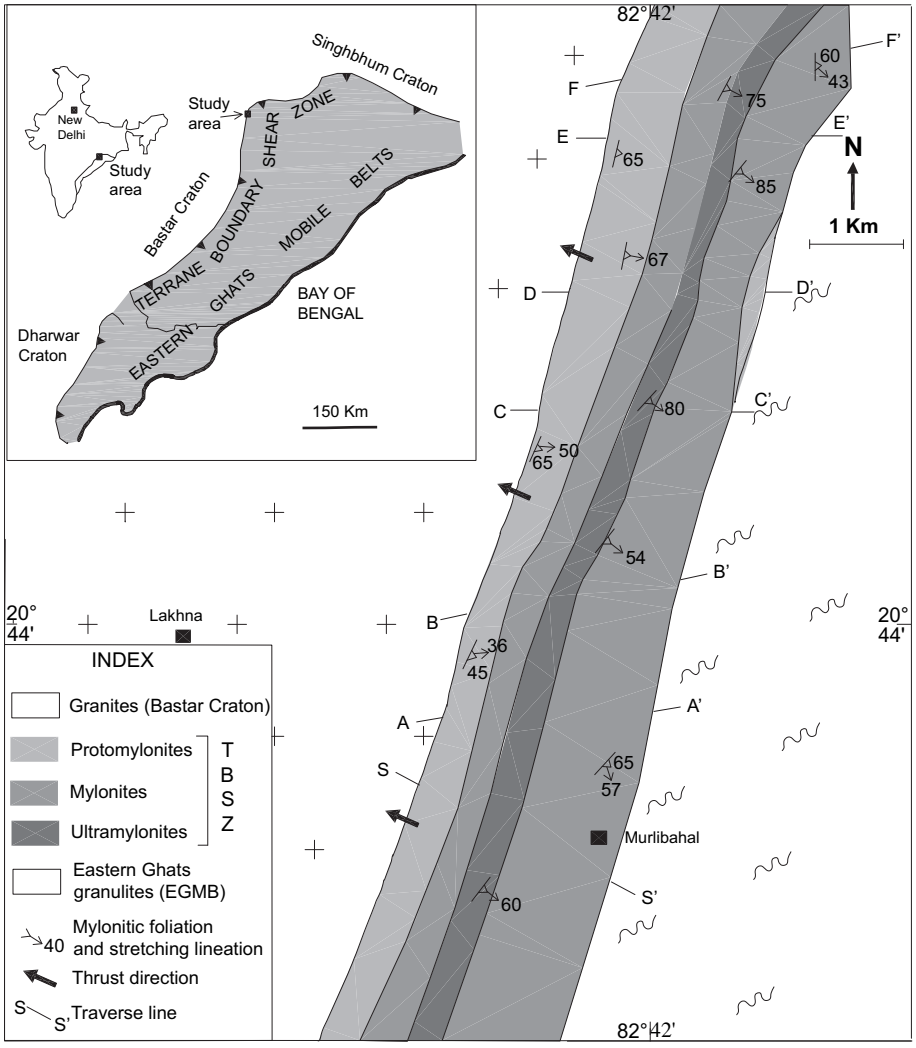

Fig. 1. Geological map of the Terrane Boundary Shear Zone (TBSZ) separating granites of the Bastor Craton in the NW from granulites of the Eastern Ghats Mobile Belt (EGMB). Seven traverses (labelled SS′, AA′, BB′, CC′, DD′, EE′ and FF′) along which the samples were collected are shown across the TBSZ east of Lakhna, India. Inset map shows the study area in relation to the Terrane Boundary Shear Zone and the Eastern Ghats Mobile Belt.

emplaced at 2.5 Ga (Sarkar et al., 1993). The TBSZ forms a 2 km wide arcuate shear zone separating these two terranes with a distinct syntaxial bend separating E–W strikes in the north from NNE–SSW trends further west (Fig. 1, *inset*). In addition, the sense of shear also varies along strike from top-to-the NW thrusting in the west to dextral strike slip in the north.

The EGMB initiated in the Archean and continued to develop into the Upper Proterozoic, although the most important event in its evolution is the Mesoproterozoic Eastern Ghats Orogeny at 1.6 Ga (Ramakrishnan et al., 1998; Mezger and Cosca, 1999). Alkaline plutons that are emplaced near the terrane margin at 517 Ma (Biswal et al., 2007), display a magmatic fabric consistent with the shear fabric present in the TBSZ, and are therefore considered coeval with thrusting and related mylonitization.

The study area lies in the NW part of the TBSZ, where the moderately inclined shear zone thrusts the EGMB over the Bastar craton by ~4 km. The craton in the study area is dominated by late tectonic granite composed of quartz, potassium feldspar, plagioclase and biotite. The rock is coarse and equigranular with occasional graphic intergrowths. There is no sign of deformation in the granite except close to the shear zone itself. The EGMB in the study area comprises charnockitic gneiss and basic granulites, which are retrogressed to amphibolites adjacent to the shear zone. The TBSZ affects both the granite of the craton and metamorphics of the EGMB. However, the fabrics are better developed in the granite due to the lack of previous deformation in these rocks, and samples were therefore collected from 7 traverses across this part (Fig. 1).

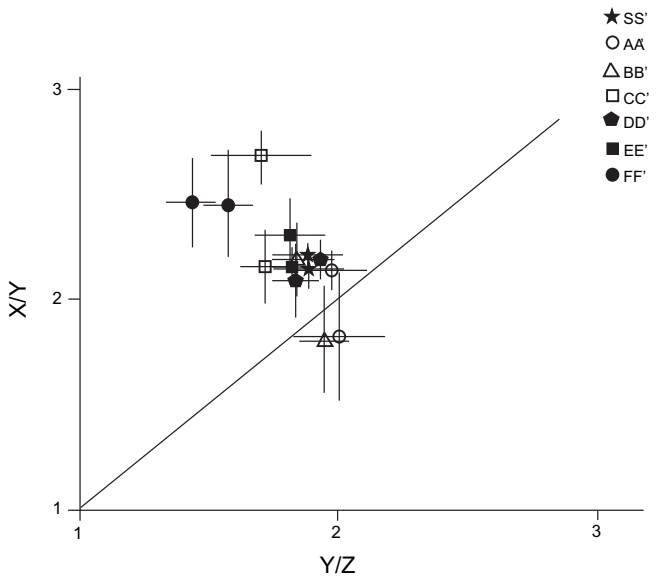

Fig. 2. Flinn diagram showing plots of the mean aspect ratios (with error bars) determined from L and T-sections of nearly 700 recrystallized quartz grains from seven different traverses (S, A, B, C, D, E, F) across the TBSZ (refer to Fig. 1 for locations of traverses). While the L-section gives the *X*/*Z* ratio, the T-section provides the *Y*/*Z* ratio. The *X*/*Y* ratio is calculated by dividing the average value of *X*/*Z* by the average *Z*/*Y* value. Although the aspect ratio varies a little, the bulk strain lies in the constrictional field indicating the effect of volume gain together with simple shear strain.

3. Nature of strain involved in the TBSZ

Traditional techniques of strain analysis have been used to examine the nature of strain in the TBSZ. Quartz grains undergo shape changes through predominantly dislocation glide and recrystallization, thus enabling estimates of the strain ellipsoid to be made from the aspect ratio of these deformed grains. Two dimensional strain measurements have been performed on mutually orthogonal planes in order to estimate the three dimensional strain. More than a hundred *X*/*Z* and *Y*/*Z* data have been collected from each of the seven traverses. The mean *X*/*Y* versus *Y*/*Z* of each sample from different traverses are plotted on a Flinn diagram (Flinn, 1962) (Fig. 2). Analysis of these data reveals that although some points fall on or near the plane strain line, the majority lie in the constrictional field. This indicates a deviation from plane strain conditions in the TBSZ which is attributed to volume gain along the shear zone (Sinha, 2004). Methods used to calculate the influence of volume gain on the state of strain include plotting the aspect ratio (*X*/*Z*) of the grains against the S–C angle (Ramsay and Huber, 1983). Using this technique, the majority of data in this analysis fall on the simple shear + dilation curve (Sinha, 2004). In addition, volume gain has also been established by undertaking a mass-balance equation using geochemical data from the mylonite samples, although the details are beyond the scope of the current paper (see Sinha, 2004). The possibility of heterogeneous transtension is considered unlikely because in transtension, the S-fabric will form a high angle with the shear zone in the central part and at lower angles toward the wall (Robin and Cruden, 1994). However, the opposite is observed in the TBSZ, where the S-fabric is at the highest angle to the C-fabric at the margin and becomes gradually parallel towards the centre (Biswal et al., 2002).

4. Microscopic structural features

Based on increasing amounts of strain, the Terrane Boundary Shear Zone (TBSZ) can be divided into three distinct structural zones, namely the protomylonite, mylonite and ultramylonite zones distributed from the outer wall to the centre of the shear zone respectively (Fig. 1). The protomylonite zone has undergone the lowest strain as suggested by the high clast to matrix ratio (70–80%), while the mylonite zone is characterized by a further reduction in grain size, and a lower clast to matrix ratio (40–50%). The ultramylonite zone is marked by extreme diminution of grain size and a low clast to matrix ratio (15–20%).

The modal percentage of different minerals present in the undeformed granite, as well as in the protomylonite, mylonite and ultramylonite, were determined manually using a point counter loaded on a binocular microscope stage. Modal composition of undeformed granite is 41% quartz, 35% orthoclase and 22% plagioclase with hornblende, biotite and sphene as accessories. Under the microscope, minor modification in the modal percentage of different minerals across the shear zone is apparent. In the protomylonite zone, quartz and feldspar constitute 43% and 47% respectively, and the remainder is mica (biotite + muscovite). In this zone, newly developed fine grained altered products such as quartz and mica form a matrix constituting 10% of the rock. With increasing alteration of mainly plagioclase and partly K-feldspar in the mylonite zone, the modal abundance is 45% quartz, 40% feldspar and 13% mica, and the remainder is epidote and opaques. The ultramylonite zone, in the central part of the shear zone, consists of 50% quartz, 30% mica and the rest is feldspar. Hence, the petrographical study indicates that although there is gradual variation in the amount of recrystallization, grain size and strain fabrics among the three zones, the basic mineralogy remains almost the same. Only the modal percentage of the minerals varies from one zone to another. This is reflected by the gradual increase of quartz and muscovite (and rarely epidote minerals), and decrease in the feldspar content from the protomylonite to ultramylonite zones. In addition, geochemical analysis of the mylonite samples from the S–S′, B–B′ and D–D′ traverses (see Fig. 1) has been carried out using the ICP-AES method which suggests an overall increase in the SiO_2% from the protomylonite to ultramylonite zone (Fig. 3, see Table 1).

Mylonite samples were collected at 150–200 m intervals along the various traverse lines (SS′, AA′, BB′, CC′, DD′, EE′ and FF′) (Fig. 1). All the mylonite samples were oriented for microscopic studies with east-side-down so that L-sections (see below) are consistently viewed towards the east. The microscopic structures are studied on both vorticity profile planes (Passchier and Coelho, 2006) or L-sections (cut parallel to stretching lineations and normal to the foliation) and T-sections (cut normal to stretching lineations).

4.1. Protomylonite zone

Outwith the TBSZ, the undeformed granite displays a typical inequigranular hypidiomorphic to xenomorphic texture in thin section (Fig. 4a). The protomylonite zone has undergone the lowest strain as suggested by the preservation of most of the feldspar grains. However, the presence of undulose extinction, deformational lamellae and lensoidal geometry of quartz grains indicates that they have undergone ductile deformation (Fig. 4b). A crude S-fabric is defined by recrystallized quartz grains. In some thin sections, micaceous layers help define the mylonitic banding or C-fabric. The rock is differentiated into alternate ductile and brittle layers made up of quartz ribbons and feldspars respectively (Fig. 4b).

The feldspar layers are composed of K-feldspar as well as plagioclase that are criss-crossed by microfractures indicating brittle deformation. However, plastic deformation is occasionally observed in the form of kinks on the twin lamellae of the plagioclase (Fig. 4c). The microfractures are shear fractures belonging to a conjugate set, and are designated as T_1 and T_2 microfractures. The 3-D orientation of the microfractures was determined by comparing the orientation of the C-fabric in L-section and from field data of the specific sample location. In L-sections, the trace of the microfractures are oblique to the C-fabric but in T-sections they are parallel to the C-fabric. So in 3-D, the strike of the microfractures are parallel to the C-fabric, with variations in the dip angle from one zone to another. Hereafter all the description of these microfractures will be based on observations in L-section. The microfractures are commonly occupied by recrystallized quartz grains arranged obliquely to the fracture wall that indicate the sense of movement along the fractures (Fig. 5a and b).

The T_1 set of microfractures, which is more prominent, is antithetic to bulk shear and is inclined in the same direction as the S-fabric. The feldspar grains have been broken by this set of fractures into a number of rectangular blocks or clasts (Fig. 5c) whose longer dimensions are also inclined in the same direction as the S-fabric. Book shelf gliding and grain-scale faults are very prominent with the microlithons showing an antithetic sense of rotation. The T_2 set of microfractures is less prominent than T_1, is inclined in an opposite sense to T_1 and is synthetic to the bulk shear.

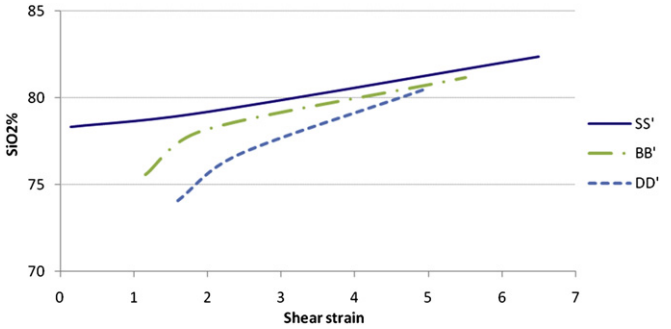

Fig. 3. Graph showing gradual increase of SiO_2% with increasing strain along the SS′, BB′ and DD′ traverses across the TBSZ.

Table 1
Average content of SiO_2 in wt% in undeformed granite (UG), protomylonite (PM), mylonite (M) and ultramylonite (UM) along three different West to East traverses (See Fig. 1 for location).

Traverse	UG	PM	M	UM	M	PM
SS'	76.74	78.34	81.34	82.36		
BB'	75.14	75.6	78.02	81.18	78.285	
DD'	71.83	73.37	73.44	80.47	80.04	74.78

Hence the bisector of the acute angle between T_1 and T_2 occurs at high angles to the C-fabric (Fig. 5a). The stereographic plot of these fractures (Fig. 6) shows a WNW to W directed sub-horizontal (5–10°) compressive stress occurring at high angles to the C-fabric. However, this orientation may not indicate the exact stress orientation as the fractures may rotate with progressive shear.

4.2. Mylonite zone

The mylonite zone is characterized by extreme reduction in grain size, higher degree of dynamic recrystallization and further differentiation of the rocks into several compositional bands. The quartz ribbons are completely polygonized with the development of dynamically recrystallized quartz grains exhibiting a distinct GSF (S-fabric) at an angle ranging between 15° and 35° from C (Fig. 7a). However, the micas forming mica rich bands are layer-parallel. Feldspar-rich layers are reduced in width as mica appears to grow at the expense of feldspar. The feldspar grains, together with the associated T_1 and T_2 shear fractures, have been rotated into variable orientations and follow the path of a rigid body (sphere) rotation. The T_1 microfractures show lower inclinations to the C-fabric (Fig. 7b), while the T_2 set has become steeper (Fig. 7c). However, the sense of shear remains the same as in the protomylonite zone. Furthermore, a greater degree of dynamic recrystallization of feldspars, quartz and mica is observed along the T_1 shear fractures, where the orientation of new grains along the fractures reflects the sense of shear. With the growth of these minerals, the separation between newly formed individual clasts has increased to produce distinct porphyroclasts. With progressive shear, the porphyroclasts assume an elliptical geometry by recrystallizing increasing amounts of material from the grain boundary. The longer axis of such clasts becomes parallel to the S-fabric, with the recrystallized material forming a distinct mantle around the grain and producing mantled porphyroclasts (Fig. 8a).

4.3. Ultramylonite zone

The ultramylonite zone is characterized by extreme diminution of grain size with very few feldspar porphyroclasts remaining intact. These float discreetly within a fine grained quartzo-feldspathic matrix (Fig. 8b). Many of the porphyroclasts display a circular shape in thin section. Discrete quartz ribbons with comparatively coarse quartz grains and an internal GSF inclined at low angles (0–10°) to the ribbon axis occur locally (Fig. 8c).

4.4. T_1 and T_2 microfractures and crystallography

In order to assess the origin of the T_1 and T_2 fractures, it is essential to know their relationship to the crystallographic axes of feldspars. This has been undertaken with respect to different twin planes and twin axes of the feldspar. Since plagioclase, orthoclase and microcline show different types of twinning, the relationship of the fractures with each of these mineral twins has been determined. Both sets of microfractures make an acute angle with the (010) Carlsbad twin plane in orthoclase (Fig. 9a). In addition, orthoclase

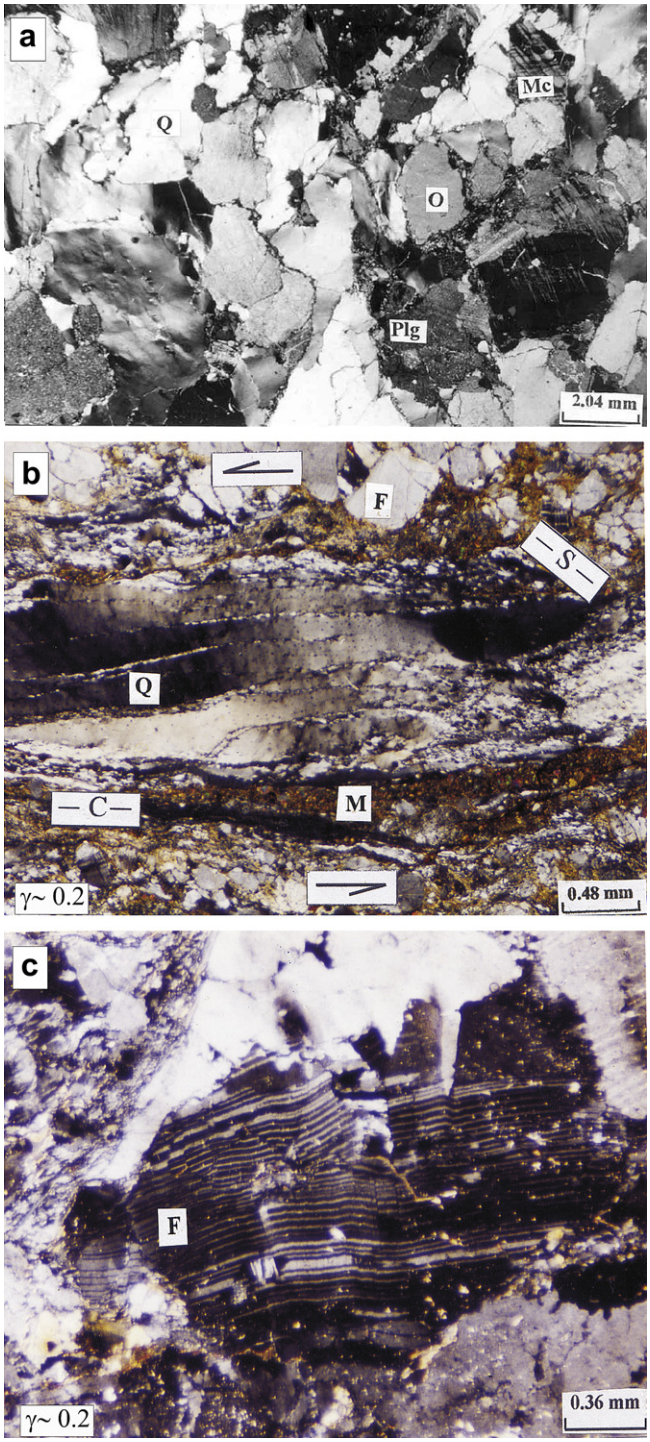

Fig. 4. Photomicrographs of (a) Granite composed of mostly quartz (Q), orthoclase (O), microcline (Mc) and plagioclase (Plg) showing a coarse-grained, inequigranular, hypidiomorphic to xenomorphic granular texture. (b) Protomylonite displaying a crude mylonitic foliation (C-fabric) comprising quartz ribbons (Q), mica layers (M) and feldspar-rich bands (F). (c) Protomylonite with kinks on the polysynthetic twin lamellae of plagioclase feldspar (F) indicating crystal plastic deformation.

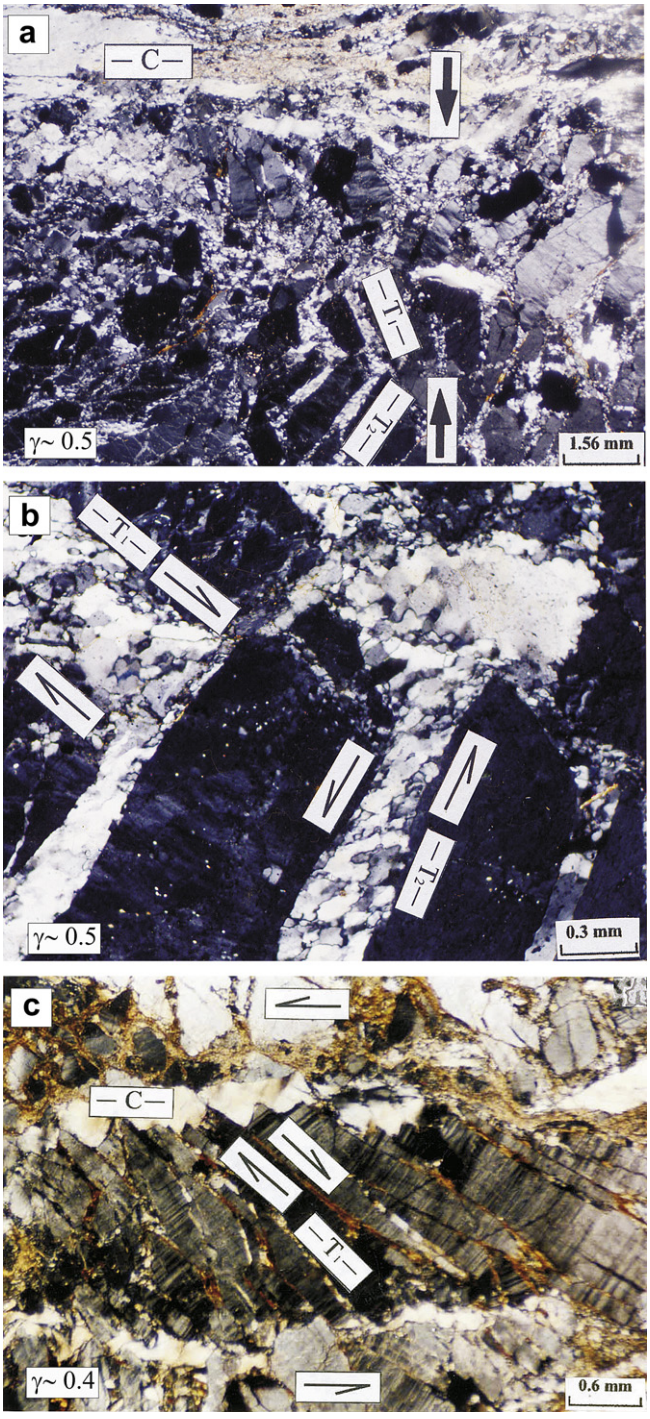

Fig. 5. Photomicrographs of (a) Protomylonite displaying the orientation of T_1 and T_2 microfractures in feldspar with respect to the C-plane. The acute angle between the T_1 and T_2 fractures indicates the direction of compression (marked by arrow). (b) T_1 and T_2 microfractures are occupied by recrystallized quartz grains arranged obliquely to the fracture wall and indicating an antithetic (dextral) sense along the T_1 set and synthetic (sinistral) sense along T_2 with respect to the anticlockwise bulk shear. (c) The T_1 and T_2 fractures have broken the larger feldspar grain into a number of smaller rectangular blocks or clasts with the T_1 fractures being inclined in a left-lateral sense.

has two sets of right angle cleavage. The T_2 fractures occur oblique to both (Fig. 9b). The prominent T_1 set of microfractures cuts across both the cleavages, i.e. (010) and (001) in plagioclase and microcline as well as the twin (albite) lamellae indicating that their origin is not crystallographically controlled. Depending on the position of the grain, the microfractures are in some places at right angles to the twin lamellae. From the pattern of albite and pericline twinning, the (010) plane of the microcline crystal can be determined and it is found that the microfractures cut across both sets of twin lamellae in microcline (Fig. 9c). Moreover the fractures make different angles with the perthite texture in feldspars (Fig. 9d). These observations

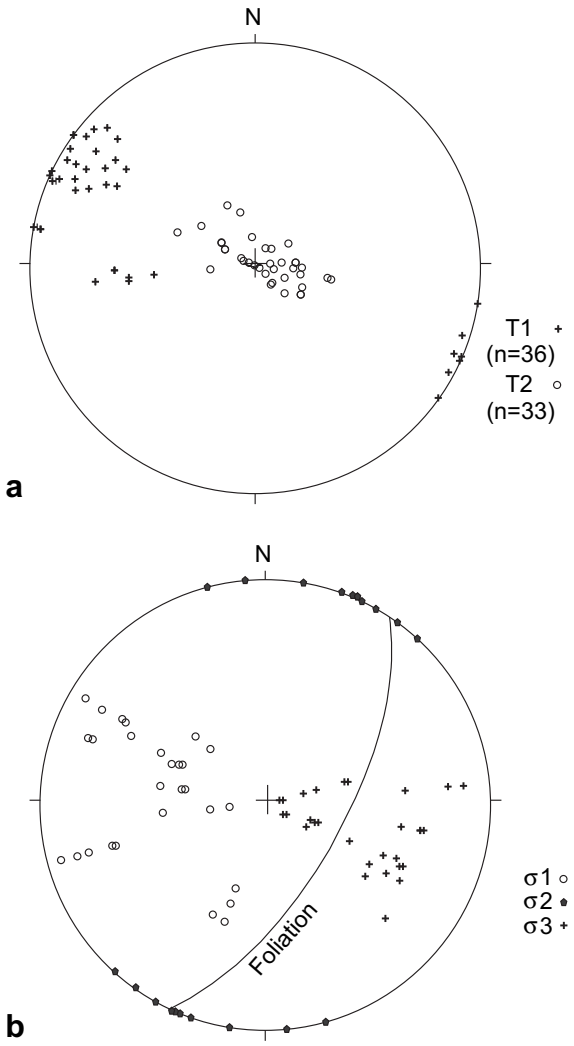

Fig. 6. (a) Stereographic projection of T_1 and T_2 fractures in protomylonite. T_1 fractures are vertical to subvertical while T_2 is horizontal to sub-horizontal. (b) Plot of σ1, σ2 and σ3 derived from the above microfractures together with a great circle representing the mean foliation. σ1 represents the maximum compressive stress oriented sub-horizontally along a WNW-ESE axis; σ2 represents intermediate stress oriented horizontally; σ3 represents the minimum compressive stress oriented moderately along an ENE axis.

indicate that the microfractures are independent of possible cleavages and crystallographic directions in all types of feldspars present in the studied mylonites.

4.5. Summary

The progressive increase in strain from the protomylonite to mylonite to ultramylonite zones is reflected by overall grain-size reduction, fall in clast to matrix ratio, progressive breaking of the feldspars, decreasing angle between S- and C-foliations and increasing elongation and dynamic recrystallization of quartz ribbons.

The overall un-changed mineralogy across the shear zone suggests that temperature and pressure have played only a very minor role, and that variation in strain is dominantly responsible for the development of the above characteristics between different zones. Results of geochemical analysis imply that the increase in modal percentage of quartz is not only due to the progressive breakdown of feldspar, but also from the direct precipitation of SiO_2 (in the form of quartz) from an external source.

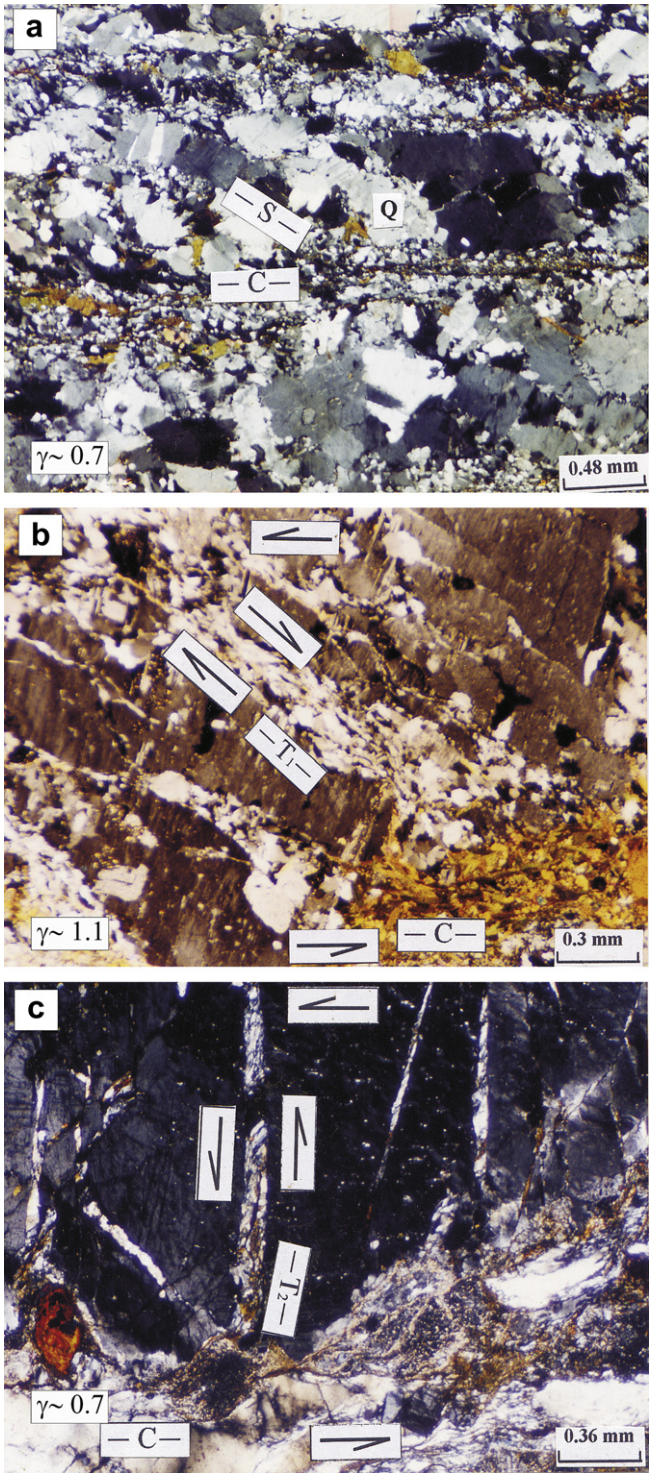

Fig. 7. Photomicrographs of mylonites. (a) Dynamically recrystallized quartz (Q) grains exhibiting distinct GSF (S-fabric) forming a 35° angle with the C-fabric. (b) The T_1 fractures showing a lower inclination to the C-fabric. The inclination of the recrystallized quartz grains within the fractures indicates an antithetic (dextral) shear along them with respect to the bulk shear. (c) The T_2 fractures show a steeper angle with respect to the C-fabric; whilst the inclination of the recrystallized quartz grains indicates a synthetic (sinistral) shear along them.

Compression at a high angle to the C-fabric suggests a pure shear deformation. However, observation of quartz ribbons in which individual grains define a grain shape fabric (GSF) oblique to the C-plane indicates the dominance of simple shear along the

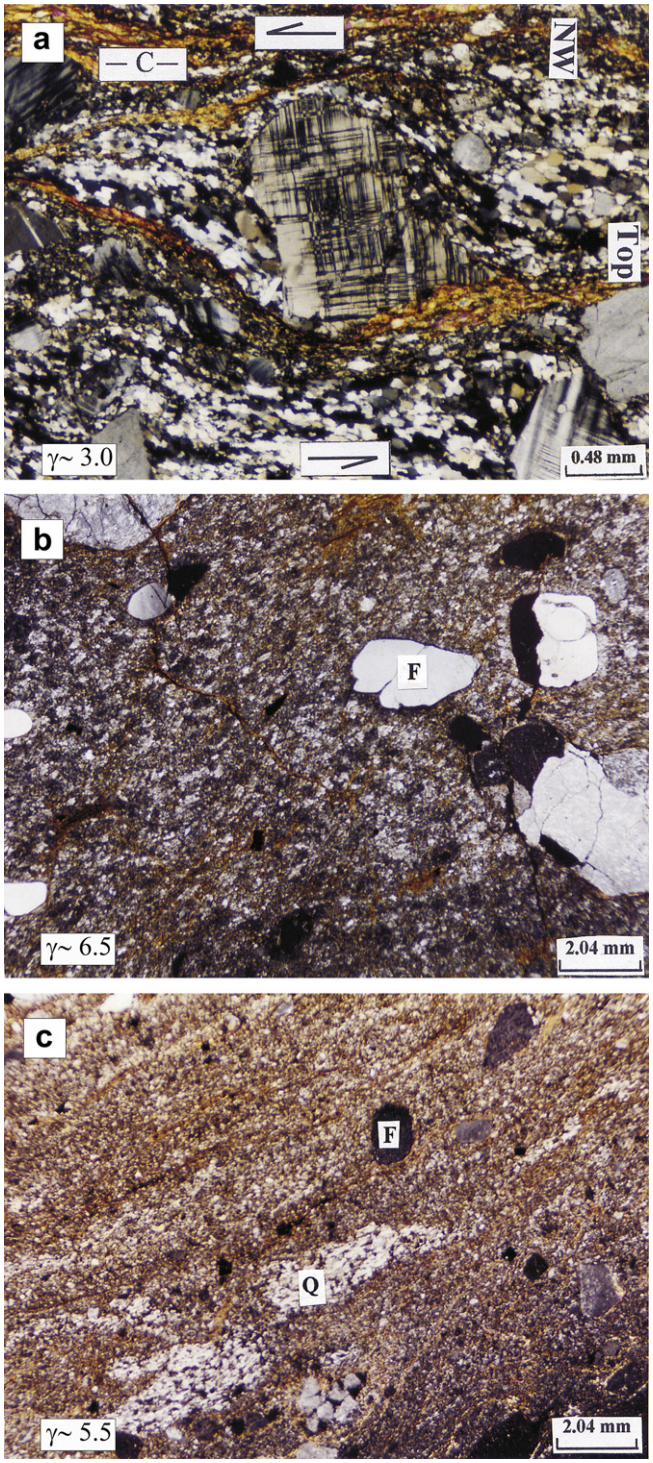

Fig. 8. Photomicrographs of mylonites and utramylonites. (a) A mantled microcline porphyroclast showing NW verging shear. The mantle is made up of finer quartz and mica grains. (b) K-feldspar (F) porphyroclasts with rounded margins occur in the fine grained matrix of an ultramylonite. (c) Discrete quartz ribbons (Q) comprising comparatively coarser polygonized quartz grains with an internal GSF inclined at a low angle to the ribbon axis. These are developed in the fine grained ultramylonite matrix. Within this matrix comparatively fewer and more rounded feldspar (F) porphyroclasts are observed.

ductile (quartz) layer. Therefore, it has been assumed that strain partitioning into simple shear and pure shear has occurred along the ductile (quartz-rich) and brittle (feldspar-rich) domains respectively (Fig. 10). The microfractures result from the pure shear component being concentrated into the relatively strong feldspar-rich layer.

The T_1 and T_2 microfractures differ from Riedel shears or *P* and *Y* shears (Davis et al., 2000) by virtue of their variable orientation relative to the C-fabric, and contrasting sense of shear. This phenomenon has been illustrated in Fig. 11 and shown in Table 2. With progressive strain, the T_1 set maintains an antithetic sense even at low angles with the C-fabric, while T_2 displays a synthetic sense in spite of being at high angles to C (Fig. 7b and c). This contrasts strongly with other fracture systems where the low angle microfractures (*R*, *Y* or *P*) show synthetic displacement and high angle ones (*R′*) show antithetic senses of shear (Fig. 11). The T_1 and T_2 microfractures not only differ from other shear fractures in orientation and sense of shear, but, along with the S-fabric, they also contribute significantly towards the development of the asymmetric fabric that is characteristic of a simple shear zone.

The T_1 set of fractures, which is the more prominent of the two, is inclined in the same direction as the S-fabric to the bulk strain. The shear microlithons produced due to parallel fracturing of the feldspar grains by T_1 are elongate parallel to the S-fabric. With progressive shear, the porphyroclasts have assumed an elliptical geometry, with the major axis lying in the same direction as the S-fabric. Further, the dynamically recrystallized grains along the fractures are also aligned along the S-fabric. The T_1 fractures originated with an antithetic sense of shear as the compression was at right angles to the C-fabric. It maintained the same sense of shear, even at low angles, in order to maintain compatibility with the S-fabric and the overall shear. This correspondence between the microfractures and the S–C-fabric suggests a kinematic control is exerted on T_1 and T_2 during their development and subsequent evolution.

The comparative study of the microfracture inclination from the protomylonite to ultramylonite zones clearly suggests a change in their angle of inclination (Table 3). The feldspar grains may also undergo many other changes, such as individual grains breaking down into smaller clasts along these fractures to assume an elliptical shape (Fig. 10). Within individual fractures, curved quartz grains display higher inclinations near the wall and lower inclinations at the centre. This suggests that the quartz grains initiated at high angles to the fracture wall, and with progressive deformation became reoriented to lower inclinations. The quartz attached to the wall cannot easily reorient and thus preserves the original angles reflecting initial strains (Fig. 12). These relationships indicate that fractures are formed in the protomylonite zone, and have variably rotated, along with the host feldspar grains, during subsequent progressive shear.

The contrasting behaviour (i.e. ductile deformation of quartz and brittle fracturing of feldspars) in the microstructure described above restricts the temperature range of ductile shearing in the TBSZ to 300–350 °C (Passchier and Trouw, 2005; Wanga and Ludmanb, 2004; Pryer, 1993). Although there is no direct evidence regarding pressure (*P*) during shearing, the quartz, feldspar, biotite and hornblende mineral assemblage in the mylonite suggests lower greenschist facies (2–2.5 kb) conditions during thrusting.

5. Fracture kinematics as a deformation mechanism

A number of assumptions were made when considering the numerical modeling of microfractures in feldspar. These include:

(i) The overall deformation involves simple shear. In the TBSZ the deformation is not strictly simple shear as volume gain causes it to deviate towards constriction. However for simplicity in theoretical calculations simple shear is assumed.
(ii) Individual feldspar grains are surrounded by a finer ductile matrix to allow easy rotation of the grain. The protomylonite

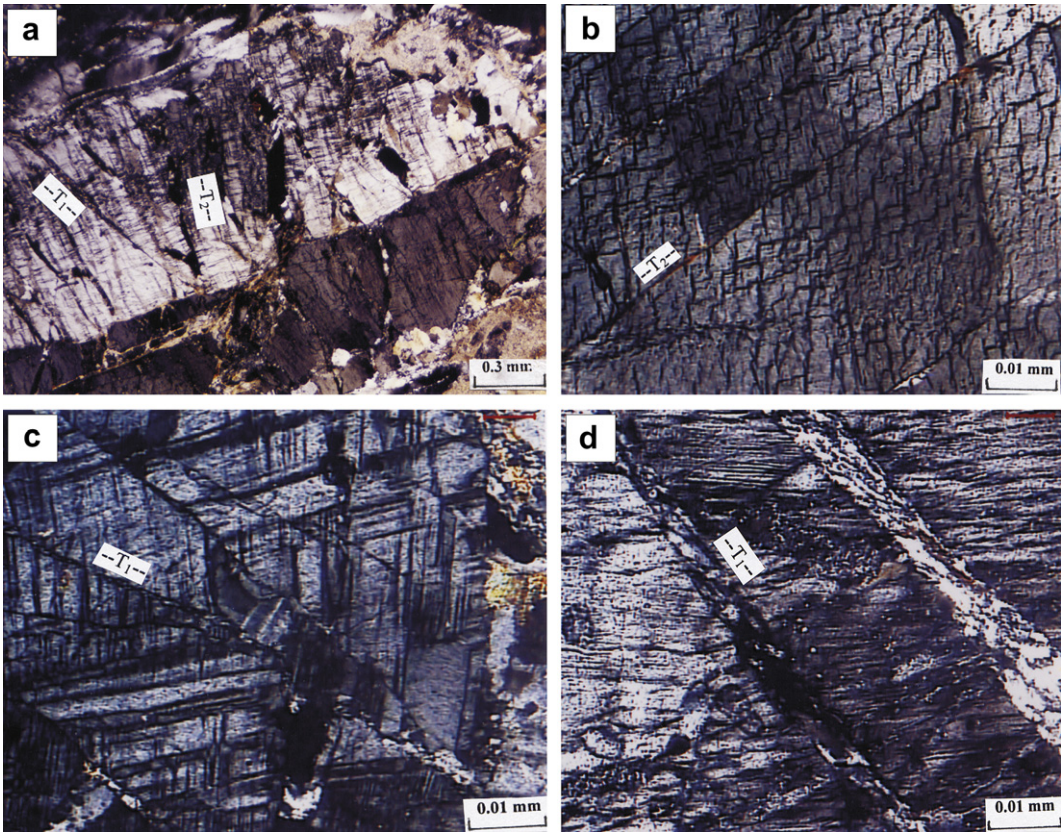

Fig. 9. Photomicrophotographs of feldspars showing relationships between twin planes, cleavage and microfractures. (a) Orthoclase showing Carlsbad twinning. The T_1 and T_2 fractures are at an angle with the twin plane. (b) Orthoclase with two sets of right angle cleavage, the T_2 fracture set is at an angle to both. (c) T_1 fractures are oblique to both sets of cross-hatched twin planes in microcline. (d) T_1 fracture cutting obliquely across the perthite intergrowth in feldspar.

zone shows the anastomosing character of the incompetent bands composed of fine mica and quartz. These bands surround the competent feldspar domains and allow the feldspar grains to undergo free rotation in the ductile quartz and mica matrix.

(iii) The feldspar grains are either circular or elliptical with low aspect ratios. From the thin section study, it has been observed that the shape of grains hosting the T_1 and T_2 sets of fractures are mostly circular, or occasionally low aspect ellipses (aspect ratio $\leq$2).

(iv) Rotation of fractures is considered up to $\gamma = 3.5$. It has been calculated from the S–C angle that the maximum shear strain in the TBSZ is $\leq$6.5. However it has been observed that at strains greater than $\gamma = 3.5$, the fractures become very wide and lose their characteristics by effectively giving rise to individual clasts.

With the above assumptions, the model we present will be valid only for a particular strain condition and any deviation from that may give a different result.

Many workers have dealt with the rotation of rigid bodies in a ductile matrix (e.g. Jeffrey, 1922; Ghosh, 1993; Ramsay and Lisle, 2000; Biermeier et al., 2001). According to their work, the equation for a rotation of an elliptical rigid body within a ductile matrix in two dimensions is as follows:

$$\omega = \overline{\gamma}\left(R^2\sin^2\alpha + \cos^2\alpha\right)/\left(R^2+1\right), \tag{1}$$

where ω is the rate of change in angle (in radians) of a marker line within an elliptical object having an aspect ratio of R, α is the initial angle that the long axis of the ellipse makes with the shear wall and $\overline{\gamma}$ is the rate of change of shear strain (Ghosh, 1993). Now, if the change in angle after rotation is φ then it can be written that:

$$\omega = \frac{d\varphi}{dt},$$
$$\text{or} \quad \omega dt = d\varphi.$$

Integrating both sides we get:

$$\begin{aligned} &\int \omega dt = \int d\varphi \\ &\text{or} \quad \omega(t'-t) = \varphi \\ &\text{or} \quad \omega = \varphi/(t'-t). \end{aligned} \tag{2}$$

Similarly, we can write:

$$\overline{\gamma} = \frac{d\gamma}{dt}.$$

After integrating as above we get:

$$\overline{\gamma} = \gamma/(t'-t). \tag{3}$$

Now replacing ω and $\overline{\gamma}$ in equation (1) by equations (2) and (3) we get:

$$\begin{aligned} &\varphi/(t'-t) = \left\{\gamma/(t'-t)\left(R^2\sin^2\alpha + \cos^2\alpha\right)\right\}/\left(R^2+1\right) \\ &\varphi = \gamma\left(R^2\sin^2\alpha + \cos^2\alpha\right)/\left(R^2+1\right). \end{aligned} \tag{4}$$

The equation of rigid body rotation of a circular object (Ghosh, 1993; Ramsay and Lisle, 2000; Biermeier et al., 2001) can be obtained from equation (4) by putting $R = 1$:

$$\varphi = \gamma/2 \tag{5}$$

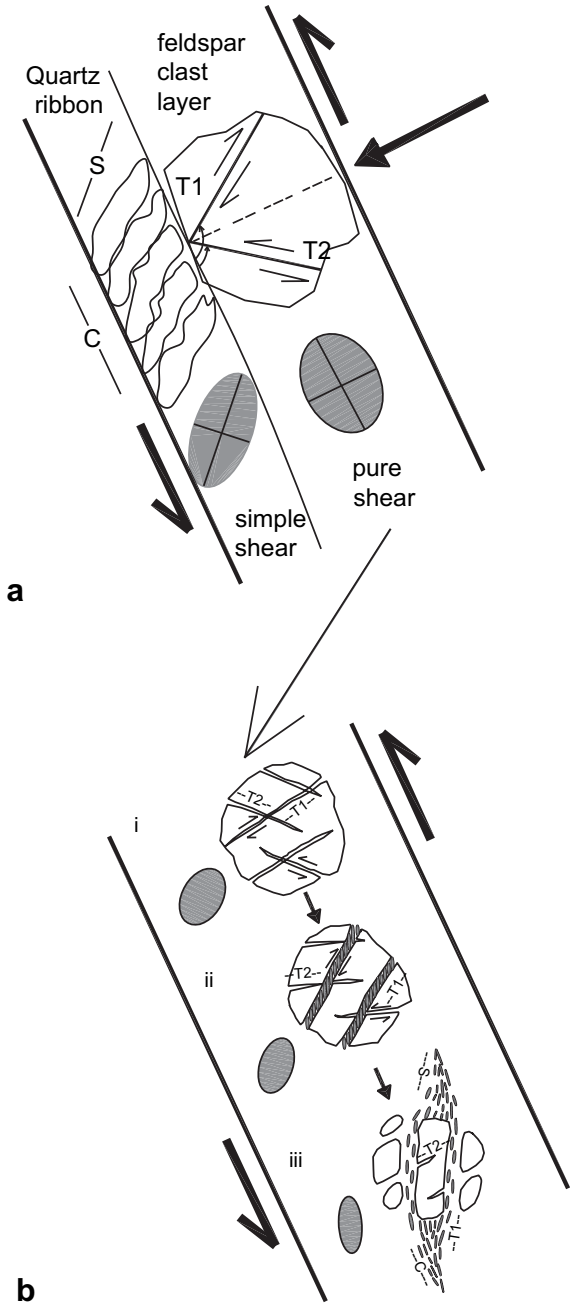

Fig. 10. Schematic diagram showing (a) strain partitioning inside the mylonite at an early stage facilitating brittle deformation of feldspar and ductile deformation in quartz dominated layers. (b) Sequential rotation of a feldspar clast during progressive simple shear. (i) T_1 and T_2 fractures with antithetic and synthetic sense of shear with respect to the main shear in the protomylonite zone. (ii) The T_1 set is preferentially widened with greater dynamic recrystallization along it. (iii) Individual clasts have been isolated and have assumed an elliptical geometry with greater recrystallization at the site of T_1 fractures.

If the marker line has an initial angle of α with the shear wall after rotation α will change over to α' measured in degrees, then from the above equation:

$$\alpha' = \alpha + (180/\pi)\varphi.$$

In the above equation putting the value of φ from equation (4) we get:

$$\alpha' = \alpha + 57.29\left\{\gamma\left(R^2\sin^2\alpha + \cos^2\alpha\right)/\left(R^2+1\right)\right\}. \quad (6)$$

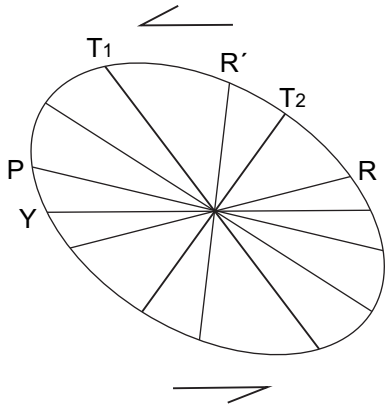

Fig. 11. Schematic cartoon illustrating the position of Riedel shears R and R', Y and P shears, and T_1 and T_2 microfractures within an overall left-lateral strain ellipse.

In the case of a circular object the aspect ratio $R = 1$. Putting this value in equation (6) we get:

$$\alpha' = \alpha + 57.29\left\{\gamma\left(R^2\sin^2\alpha + \cos^2\alpha\right)/2\right\}.$$

Putting $(\sin^2\alpha + \cos^2\alpha) = 1$ we get:

$$\alpha' = \alpha + 28.64\gamma \quad (7)$$

In the present case the elliptical grains have a maximum aspect ratio of 2, so it is considered that $R = 2$. Putting this value in equation (6) we get:

$$\alpha' = \alpha + 57.29\left\{\gamma\left(4\sin^2\alpha + \cos^2\alpha\right)/(4+1)\right\},$$
$$\text{or} \quad \alpha' = \alpha + 11.46\gamma\left(4\sin^2\alpha + \cos^2\alpha\right) \quad (8)$$

Further, the shear along the fractures is controlled by the bulk shear strain and the initial inclination. This can be shown by the following equation (Nadai, 1963):

$$\gamma_f = 1/2\gamma^2\sin2\alpha + \gamma\cos2\alpha, \quad (9)$$

where γ_f = shear along the microfracture, γ = bulk shear and α = angle of inclination of the fracture to the C-plane.

Table 2
Summary of Riedel and T_1 and T_2 fracture characteristics.

R–R' Fractures	T_1–T_2 Fractures
Riedel fractures occur in conjugate sets termed R and R'. R forms low angles (10–15°) to the C-fabric while R′ is at high angles (75–80°).	T-fractures occur in conjugate sets termed T_1 and T_2. Both form moderate (acute) angles to the C-fabric. T_1 makes angles of 54° while T_2 forms at 72° with the shear plane. The acute angle between T_1 and T_2 faces towards the C-plane.
R (at relatively low angles with the shear plane) shows a synthetic sense of shear with the bulk shear. R' (at relatively high angles with the shear plane) shows antithetic shear.	T_1 (at relatively lower angles with the shear plane) shows an antithetic sense of shear with the bulk shear. T_2 (at relatively higher angles with the shear plane) shows synthetic shear.
The angle between R and R' is such that the acute bisector remains close to the shortening direction of the strain ellipse for the incremental strain.	The T_1–T_2 conjugate set is the result of brittle fracturing, where the compression direction is the acute bisector of the conjugate (following Andersonian theory).

Table 3
Angular relation of T_1 and T_2 microfractures with respect to the C-fabric as seen in the vorticity profile plane in thin sections from the seven traverses. The sample prefix reflects the traverse (see Fig. 1).

Sample No.	T1^C	T2^C	Sample No.	T1^C	T2^C
S3	106	48	D2	106	49
S4	110	51	D3	110	70
S5	112	52	D4	132	90
S7	121	61	D4	144	97
S10	181	121	D5	160	122
S11	159	98	D5	167	125
S13	124	66	D6	170	130
A4	100	45	D11	106	67
A5	103	43	E3	128	78
A6	109	42	E4	132	92
A7	115	65	E5	135	95
A9	165	115	E6	151	107
A11	120	85	E6	150	110
A12	130	55	E9	122	82
B3	108	48	E13	112	72
B3	110	52	F3	107	39
B4	117	70	F3	110	45
B5	130	77	F3	122	58
B6	160	110	F4	125	62
B10	158	90	F4	125	65
B12	120	63	F4	127	66
C3	120	65	F4	132	75
C4	140	85	F5	136	78
C5	160	105	F5	137	74
C8	155	100	F5	145	80
C9	145	90	F6	148	98
			F8	155	107
			F10	160	110

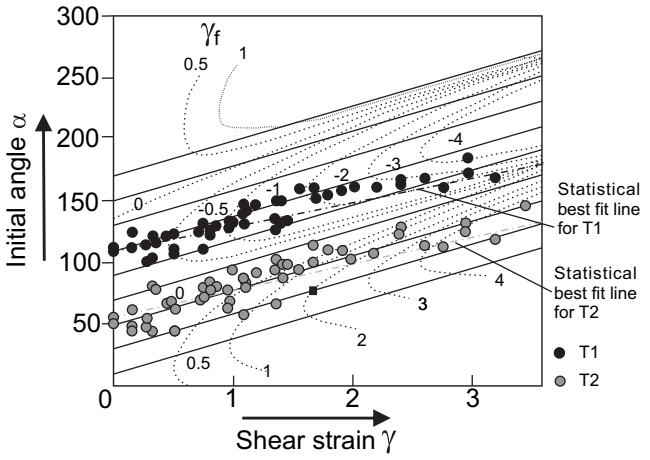

Fig. 13. $\gamma-\alpha$ graph showing the rotation paths of circular objects (continuous black straight lines) undergoing simple shear. α is the initial angle of inclination of the fractures with the shear wall inside such objects and γ is the bulk shear strain. γ_f is the shear strain along the fractures plotted as curved dashed lines. The statistical best fit for T_1 and T_2 rotation paths (continuous grey lines) illustrate the rotation of the fractures as observed in thin sections. These are plotted by measuring the angles that T_1 and T_2 fractures make with the mylonitic foliation at different values of γ. The best-fit line is extrapolated towards the *Y* axis to get the initial angle of inclination. The initial angle for T_1 and T_2 is found to be 108° and 54° respectively. The γ values are calculated using the S^C angle. The statistical best-fit line for T_1 and T_2 fractures forms a small angle with the ideal rotation path, which is interpreted to be the result of volume gain.

Two graphs have been plotted comparing γ and α, one for T_1 and T_2 microfractures hosted in circular objects (Fig. 13) and the other for microfractures in elliptical objects (Fig. 14). In Fig. 13 the rotation paths of circular objects have been drawn following equation (7) whilst in Fig. 14 the rotation paths of elliptical objects with aspect ratio 2 have been drawn following equation (8). The first graph (Fig. 13) shows a set of straight and parallel (continuous) black lines with a positive slope while the second graph (Fig. 14) shows nonparallel straight (continuous) black lines. These lines represent the rotation paths of circular and elliptical objects hosting the microfractures. Over these, a second set of (dashed) curves have been superimposed to show the variation of γ_f with different values of γ and α using equation (9). It shows both +ve and −ve values for left lateral and right lateral shear. The zero line separates the two fields. In each of the graphs, these two families of curves together illustrate the variations in orientation of fractures, together with the magnitude and sense of shear along them at various levels of bulk shear strain. It therefore follows that, if one can measure γ and α' from any natural shear zone sample, it is possible to determine the corresponding α and γ_f values from these graphs. Any point on the graph enables the two variables (α and γ_f) to be directly read off from the two sets of intersecting curves.

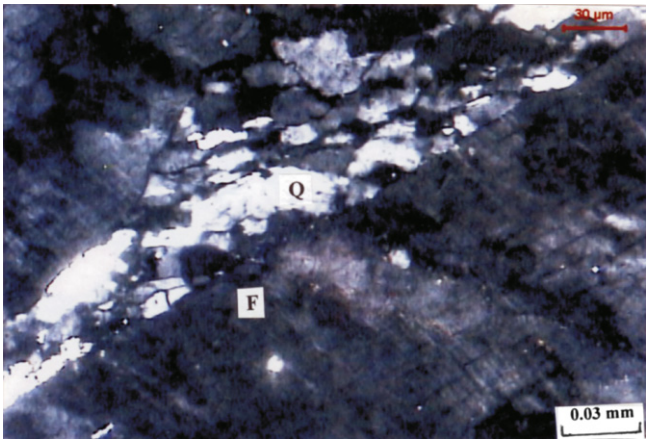

Fig. 12. Curved quartz grains (Q) contained within T_2 fractures in feldspar (F) have a higher inclination near the wall and a lower inclination in the central part of the fracture suggesting a rotation of the T_2 fracture from the protomylonite to mylonite zones.

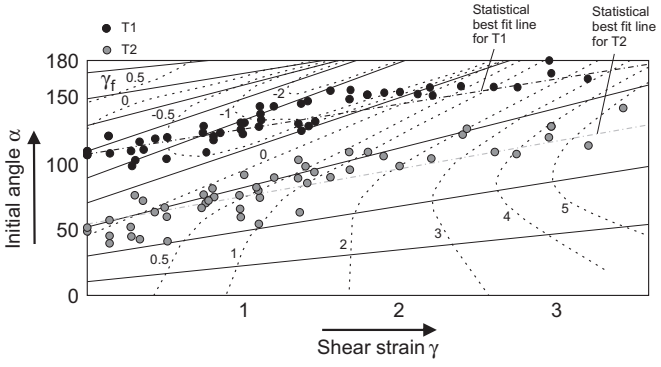

Fig. 14. $\gamma-\alpha$ graph showing rotation paths of elliptical objects (continuous black lines) undergoing simple shear. α is the initial angle of inclination of the fractures with the shear wall inside such objects and γ is the bulk shear strain. γ_f is the shear strain along the fractures plotted as curved dashed lines. The statistical best fit for T_1 and T_2 rotation paths (grey continuous line) illustrate the rotation of the fractures as observed in thin sections. These are plotted by measuring the angles that T_1 and T_2 fractures make with mylonitic foliation at different values of γ. The best-fit line maintaining the slope of the rotation path of the ellipse is extrapolated towards the *Y* axis to get the initial angle of inclination. Initial angles of T_1 and T_2 fractures are found to be 108° and 54° respectively. The γ values are calculated using S^C angles. The statistical best-fit line for T_1 and T_2 fractures shows a small deviation because of volume change involved with simple shear.

5.1. Characteristics of the graphs

5.1.1. Graphs for fractures hosted in circular objects (Fig. 13)

(i) The fracture rotation paths for circular grains are mutually parallel indicating a constant rate of rotation of the porphyroclasts irrespective of their initial orientations.
(ii) The fractures can rotate by any amount and hence may pass through the shear plane to the opposite side. Thus the exact amount and sense of rotation cannot be known from the particular position of a fracture in a progressive shear.
(iii) Depending on the field of the γ_f, a particular rotation path will have either +ve or −ve shear sense. At $\gamma_f = 0$, it has no shear. Hence the shear sense largely depends on the initial angle. A fracture originating with a high angle may maintain its sense of shear even after rotating to a low angle with C. For example this relationship is seen with initial angle 90°.
(iv) Depending on the initial angle, the magnitude of shear can be greater than the bulk shear. For example a fracture with $\alpha = 30°$ will assume α' at point F. At this position the $\gamma_f = 2$ while γ is 1.7. This highlights the dependence of shear strain along a fracture on its initial angle with the shear wall.

5.1.2. Graphs for fractures hosted in elliptical objects (Fig. 14)

(i) The graph shows that fracture rotation paths hosted in elliptical grains with constant aspect ratio are not parallel. This depicts variable rates of rotation of the porphyroclasts depending on their initial orientations.
(ii) Beyond 180° (initial angle) with the C-plane, the rotation paths intersect one another indicating a very complex nature of rotation. If any α' versus γ plot falls on such an intersection point, it is not possible to read a unique initial α for it from the graph. So for simplicity the field of the graph is restricted up to 180° only.
(iii) Depending on the field of the γ_f, a particular rotation path will have either +ve or −ve shear sense (as in Fig. 13). At $\gamma_f = 0$, it has no shear. Hence the shear sense largely depends on the initial angle. A fracture originating with high angles may maintain its sense of shear even after rotating to a low angle with the C-plane.
(iv) Depending on the initial angles, the magnitude of shear along the fractures can be lower, equivalent to, or even higher than the bulk shear. So as with circular objects, the magnitude of shear along the fractures in elliptical objects is controlled by the initial orientation of the fractures with respect to the C-plane.

5.2. Fracture kinematics of the studied samples

As the TBSZ is a low temperature shear zone, the rate of recrystallization to reset the finite stain clock is relatively slow. Thus, the resulting GSF is less able to keep up with the instantaneous strain and accurately reflect the finite strain (Davis and Reynolds, 1996). So, assuming simple shear, the finite strain values (γ) have been calculated from S to C angles (measured from thin sections) following the Ramsay and Huber (1983, 1987) equation:

$$\gamma = 2\cos 2\theta, \tag{10}$$

where θ is the S–C angle measured in degrees.

These γ values, along with the observed α' for T_1 and T_2 fractures, have been plotted in both the graphs (Figs. 13 and 14). In the graph for fractures hosted in circular grains (Fig. 13) the best-fitting curve gave initial angles of 108° and 54° for T_1 and T_2 respectively (measured anticlockwise). The statistical best-fit line passing through the measured value from the thin section shows a lower rate of rotation (grey continuous line) for the rigid object with respect to the rotation path of a rigid body under only simple shear. The statistical best-fit lines for T_1 and T_2 have slopes 5° less than the above lines. In the case of fractures hosted in elliptical objects, the best-fitting curve (grey continuous line) through the plots for T_2 shows slopes 3° less with respect to the rotation path of the elliptical object under simple shear (Fig. 13). This angular deviation may be due to volume gain across the shear zone (Sinha, 2004). The amount of rotation towards the shear direction of a passive marker line is proportional to γ and inversely proportional to volume gain. The resultant rate of rotation of the passive marker line will be less under combined simple shear and volume gain relative to that of simple shear alone.

Thus in a shear zone where both shear strain (γ) and volume increase are increasing progressively, the resultant vector at each stage of the increment will lead to a lesser amount of rotation of the passive marker towards the shear direction than would occur under simple shear only. This may explain the reason for the deviation of the best-fit line from the theoretical rotation path of the elliptical rigid object. In the case of circular objects, theoretically dilation does not affect the rotation but the grains, after a little rotation, achieve some aspect ratio and may follow the rotation path of an ellipse and are affected by the dilation.

The T_1 curve in Fig. 13 lies in the −ve γ_f sector throughout the deformation ($\gamma \leq 3.5$), while the T_2 curve in both graphs (Figs. 13 and 14) lies in the +ve γ_f sector throughout the deformation. This leads to the inference that, the T_1 and T_2 fractures will undergo right and left lateral shear respectively. Further, they will not change their sense of shear until the highest strain ($\gamma = 3.5$). Even at low angles to the C-fabric, T_1 fractures will show a right lateral sense (Fig. 7b). On the other hand, the T_2 curve throughout the deformation lies in the +ve γ_f sector. The thin section study suggests a left-lateral sense of shear along it even when it is at high angles with the shear wall (Fig. 7c). Considering both graphs, the shear strain along the T_2 fractures is less than, or equivalent to, the bulk shear up to $\gamma = 2$, and then it increases to more than the bulk shear. Conversely, the magnitude of shear strain along T_1 fractures is more than the bulk shear even at $\gamma = 0.5$. Comparing the magnitude of shear along T_1 and T_2 fractures from the graphs, it is apparent that throughout the deformation process the magnitude of γ_f along T_1 is higher than T_2 and even greater than the bulk shear. This fact explains the dominance of T_1 fractures over T_2 fractures, and also the typical breakdown of feldspar grains along the T_1 fracture set.

6. Discussion

This study has involved analysis of microstructures from the TBSZ, and a comparison of these structures with numerical models for microfracture rotation under progressive shear. With the initiation of thrusting, the feldspar and quartz start to segregate into separate brittle and ductile layers respectively (even at very low strains). Due to this competency contrast, strain partitioning takes place with simple shear focused into the quartz and mica dominated layers, and pure shear in the feldspar dominated layers. In response to the dominant pure shear component, individual feldspar grain undergo brittle fracturing following Anderson's model. The position of the acute bisectrix between T_1 and T_2 lies at a high angle to the C-fabric, although it is not perpendicular to it. This can be explained by the influence of a component of simple shear inside the feldspar domain. In the protomylonite zone,

where T_1 and T_2 fractures are first visible, they are closed fractures. With progressive shear the microfractures change their orientation due to the rotation of the host feldspar grains. The feldspar grains rotate as rigid objects within the ductile matrix of fine recrystallized quartz and mica. During rotation, the T_1 set experiences large strain concentrations on gliding planes because of its parallelism with the S-fabric. A book shelf gliding structure is commonly seen along these fractures. This leads to the removal of more and more material from the edge of the clasts, and their subsequent chemical breakdown to quartz and mica producing mantle structures. In addition, quartz derived from an external source is precipitated within the microfractures, also facilitating the fracture widening process. As a consequence, the original grain gets split into individual clasts. Again as these clasts are produced due to parallel fracturing of the feldspar grains by T_1 microfractures, they are elongated parallel to the S-fabric. With progressive shear, the porphyroclasts have assumed an elliptical geometry with major axes lying in the same direction as the S-fabric. Further, the dynamically recrystallized quartz grains along the fracture are also aligned according to the shear acting along those fractures i.e. left lateral in T_2 and right lateral in T_1. The nature of fracture rotation observed in the theoretical modeling points to a kinematic control acting during the development and subsequent evolution of the microfracture set in the following manner:

(i) The antithetic or synthetic sense of shear along the microfracture with respect to the bulk shear does not depend on the magnitude of its finite inclination with the C-fabric, but on the amount of the initial angle. Thus, a low angle fracture may show an antithetic relationship if it originates at high angles; or a sympathetic relationship can be observed along high angle fractures if they originate at low angles with the shear wall. In addition, there is a set of curves that would show a change in shear sense with progressive shear. For example in Fig. 13 the rotation path of $\alpha = 70$ jumps over the $\gamma_f = 0$ line at $\gamma = 2.4$ from an antithetic to a synthetic sense. Similar observations for the $\alpha = 150$ path occur at $\gamma = 1.15$ where the shear sense changes from synthetic to antithetic.

(ii) The development of microfractures in the brittle (feldspar-rich) layer, the dominance of a particular set, and the magnitude of shear strain along them are controlled by overall shear strain. The brittle layer breaks along conjugate fracture sets in such a fashion that one of the sets will be inclined with a specific angle in the same direction as the S-fabric. That particular set gains dominance over the other. The magnitude of shear strain along that set is also greater than the other and even compares to the bulk shear. Hence breaking down of the grain and development of clasts is facilitated in that direction. The porphyroclasts also assume an ellipticity with the longer dimension in that direction.

(iii) The graphs (Figs. 13 and 14) are useful to determine the initial angle of the microfracture with respect to the C-fabric even from a strained sample (knowing the finite strain along the microfracture at any stage of progressive deformation) where the microfractures are already rotated. This in turn may be used to determine the bulk sense of shear, and may be helpful in particular cases where bulk sense of shear cannot be determined confidently from other observations.

7. Conclusion

The Terrane Boundary Shear Zone displays a variety of mylonitic fabrics that suggest oblique thrusting towards the NW during lower greenschist facies conditions. The microfractures (here designated T_1 and T_2) produced in the feldspar clasts during thrusting are a consequence of strain partitioning into layers of different competence. The T_1 and T_2 microfractures occur in conjugates with T_1 inclined in the same direction as the S-fabric and showing an antithetic sense to the NW verging shear, while T_2 is inclined in an opposite sense to the S-fabric and displays synthetic shear. As T_1 is inclined at low angles to the *XY* plane and in the same direction as the S-fabric, it undergoes maximum shear strain compared to T_2 and may even exceed the bulk shear. This aids in breaking down the feldspar grains as well as their dynamic recrystallization, and facilitates formation of asymmetric shear fabrics. The T_1 set maintains an antithetic sense of shear even at low angles with the C-fabric, while T_2 displays a synthetic sense in spite of being at high angles to C. The T_1 and T_2 fractures therefore differ significantly from the classic Riedel, *P* and *Y* shears where low angle fractures display synthetic shear and high angle ones (R') show antithetic displacement with respect to the bulk shear sense.

Acknowledgements

We thank the late Prof. S. K. Ghosh (J.U., Kolkata) for his suggestions and help with this work. We are also thankful to the Department of Earth Science, IIT-Bombay and CSIR, New Delhi, India for their financial help, together with Sandra Piazolo and Kyu Kanagawa for careful and constructive reviews.

References

Biermeier, C., Stüwe, K., Barr, T.D., 2001. The rotation rate of cylindrical objects during simple shear. Journal of Structural Geology 23, 765–776.
Biswal, T.K., Sajeevan, G., Nayak, B.P., 1998. Deformational history of eastern Ghats mobile belt around Lathore, Balangir district, Orissa. Journal of Geological Society of India 51, 219–225.
Biswal, T.K., Biswal, B., Mitra, S., Roy Mulik, M., 2002. Deformation pattern of the NW terrane boundary of the Eastern Ghats Mobile Belt, India. A tectonic model and correlation with Antarctica. Gondwana Research 5, 45–52.
Biswal, T.K., Sinha, S., 2003. Deformation history of the NW salient of the eastern Ghats mobile belt, India. Journal of Asian Earth Sciences 22, 157–169.
Biswal, T.K., Sinha, S., 2004. Fold-Thrust-Belt structure of the eastern Ghat mobile belt; A line of correlation between India and Antarctica in Gondwana. Gondwana Research 7, 43–56.
Biswal, T.K., De Waele, B., Ahuja, H., 2007. Timing and dynamics of the juxtaposition of the Eastern Ghats Mobile Belt against the Bhandara Craton, India: a structural and zircon U-Pb SHRIMP study of the fold-thrust belt and associated nepheline syenite plutons. Tectonics 26, TC4006. doi:10.1029/2006TC002005.
Davis, G.H., Reynolds, S.J., 1996. Structural Geology of Rocks and Regions. John Wiley and Sons. Inc., New York, pp. 545–546.
Davis, G.H., Bump, A.P., Garcia, P.E., Ahlgren, S.G., 2000. Conjugate Riedel deformation band shear zones. Journal of Structural Geology 22, 169–190.
Druguet, E., Alsop, G.I., Carreras, J., 2009. Coeval brittle and ductile structures associated with extreme deformation partitioning in a multilayer sequence. Journal of Structural Geology 31, 498–511.
Flinn, D., 1962. On folding during three dimensional progressive deformations. Quarterly Journal of Geological Society 118, 385–433.
Ghosh, S.K., 1993. Structural Geology: Fundamentals and Modern Developments. Pergammon press, Oxford, p. 597.
Goodwin, L.B., Tikoff, B., 2002. Competency contrast, kinematics, and the development of foliations and lineations in the crust. Journal of Structural Geology 24, 1065–1085.
Hirth, G., Tullis, J., 1992. Dislocation creep regimes in quartz aggregates. Journal of Structural Geology 14, 145–159.
Jeffrey, G.B., 1922. The motion of ellipsoidal particles in a viscous fluid. Proceedings of the Royal Society of London 102, 161–179.
Lister, G.S., Snoke, A.W., 1984. S-C mylonites. Journal of Structural Geology 6, 617–638.
Mezger, K., Cosca, M.A., 1999. The thermal history of the Eastern Ghats belt (India) as revealed by U-Pb and $^{40}AR/^{39}Ar$ dating of metamorphic and magnetic minerals: implications for SWEAT correlation. Precambrian Research 94, 251–271.
Nadai, A., 1963. Theory of Flow and Fractures of Solids, vol. 2. McGraw-Hill, New York, p. 705.
Park, Y., Yoo, S., Ree, J., 2006. Weakening of deforming granitic rocks with layer development at middle crust. Journal of Structural Geology 28, 919–928.

Passchier, C.W., Coelho, S., 2006. An outline of shear-sense analysis in high-grade rocks. In: Chetty, T.R.K., Fitzsimons, I.C.W., Brown, L.D., Dimri, V.P., Santosh, M. (Eds.), Mem. Gondwana Research, Crustal Structure and Tectonic Evolution of the Southern Granulite Terrain, India, pp. 66–76.

Passchier, C.W., Trouw, R.A.J., 2005. Micro-tectonics, second ed. Springer-Verlag, Berlin, Heidelberg, 366 pp.

Petit, J.P., 1987. Criteria for the sense of movement on fault surfaces in brittle rocks. Journal of Structural Geology 9, 597–608.

Pryer, L.L., 1993. Microstructures in feldspars from a major crustal thrust zone: the Grenville Front, Ontario, Canada. Journal of Structural Geology 15, 21–36.

Ramakrishnan, M., Nanda, J.K., Augustine, P.F., 1998. Geological evolution of the Proterozoic eastern Ghats mobile belt. Geological Survey of India Special Publication 44, 1–21.

Ramsay, J.G., Huber, M.I., 1983. The Techniques of Modern Structural Geology. In: Strain Analysis, vol. 1. Academic press, London, p. 296.

Ramsay, J.G., Huber, M.I., 1987. The Techniques of Modern Structural Geology. In: Folds and Fractures, vol. 2. Academic press, London, p. 686.

Ramsay, J.G., Lisle, R., 2000. The Techniques of Modern Structural Geology. In: Application of Continuum Mechanics in Structural Geology, vol. 3. Academic press, London, p. 856.

Robin, P.Y.F., Cruden, A.R., 1994. Strain and vorticity patterns in ideally ductile transpressional zones. Journal of Structural Geology 16, 447–466.

Sarkar, G., Corfu, F., Paul, D.K., Mcnaughton, N.J., Gupta, S.N., Bishul, P.K., 1993. Early Archean crust in bastar craton, Central India – a geochemical and isotopic study. Precambrian Research 62, 127–137.

Simpson, C., Schmid, S.M., 1983. An evaluation of criteria to determine the sense of movement of sheared rocks. Bulletin of the Geological Society of America 94, 1281–1288.

Sinha, S., 2004. Strain analysis of the Terrane Boundary Shear Zone developed between the Bastar Craton and the Eastern Ghats Mobile Belt, around Lakhna, Nawapara district, Orissa, India. Unpub. Ph.D. thesis, IIT-Bombay, India.

Wanga, C., Ludmanb, A., 2004. Deformation conditions, kinematics, and displacement history of shallow crustal ductile shearing in the Norumbega fault system in the Northern Appalachians, eastern Maine. Tectonophysics 384, 129–148.